applied sciences

MDPI

Article

High-Precision Noncontact Guided Wave Tomographic Imaging of Plate Structures Using a DHB Algorithm

Junpil Park [1], Jaesun Lee [2], Zong Le [3] and Younho Cho [1,*]

1 School of Mechanical Engineering, Pusan National University, Busan 46241, Korea; jpp@pusan.ac.kr
2 School of Mechanical Engineering, Changwon National University, Changwon 51140, Korea; jaesun@changwon.ac.kr
3 National Deep Sea Center, Ministry of Natural Resources, Qingdao 266247, China; zongl@ndsc.org.cn
* Correspondence: mechcyh@pusan.ac.kr; Tel.: +82-51-510-2323

Received: 26 May 2020; Accepted: 24 June 2020; Published: 25 June 2020

Abstract: The safety diagnostic inspection of large plate structures, such as nuclear power plant containment liner plates and aircraft wings, is an important issue directly related to the safety of life. This research intends to present a more quantitative defect imaging in the structural health monitoring (SHM) technique by using a wide range of diagnostic techniques using guided ultrasound. A noncontact detection system was applied to compensate for such difficulties because direct access inspection is not possible for high-temperature and massive areas such as nuclear power plants and aircraft. Noncontact systems use unstable pulse laser and air-coupled transducers. Automatic detection systems were built to increase inspection speed and precision and the signal was measured. In addition, a new Difference Hilbert Back Projection (DHB) algorithm that can replace the reconstruction algorithm for the probabilistic inspection of damage (RAPID) algorithm used for imaging defects has been successfully applied to quantitative imaging of plate structure defects. Using an automatic detection system, the precision and detection efficiency of data collection has been greatly improved, and the same results can be obtained by reducing errors in experimental conditions that can occur in repeated experiments. Defects were made in two specimens, and comparative analysis was performed to see if each algorithm can quantitatively represent defects in multiple defects. The new DHB algorithm presented the possibility of observing and predicting the growth direction of defects through the continuous monitoring system.

Keywords: tomographic imaging; DHB algorithm; noncontact; air-coupled transducer

1. Introduction

It is well known that Lamb waves can propagate long distances with little energy loss. Lamb waves have been shown to be sensitive to most types of defects. They are also efficient for detecting tiny subsurface damages and inspecting large areas. Such noncontact nondestructive testing (NDT) methods have great advantages for online inspection because high temperature or other negative factors can restrict the application of contact methods. In earlier research, ultrasonic Rayleigh and Lamb waves were used to reconstruct images in metal plates using water immersion techniques [1]. Other studies have used electromagnetic acoustic transducer (EMAT)-based methods [2–4] and contact techniques [5–9]. Air-coupled transducers have been used for tomography imaging since the end of the last century [10]. The application of purely air-coupled transducers has always been limited for the detection of nonmetallic materials [11,12] due to the high acoustic impedance between air and solid materials. Other methods, such as disc sensors, have also been widely used for the detection of

metallic materials [13], but those methods are not truly noncontact methods. The research team of Rymantas J. K. developed PMN-PT synthesized with lead magnesium niobate–lead titanate crystals, and applied PMN-PT, which has a strong piezoelectric effect, to an air-coupled transducer to improve performance [14,15]. Therefore, it is believed that the hybrid application of a pulse laser and air-coupled transducer will have good performance as a fully noncontact detection system [16,17].

Most of the works mentioned above are based on the traditional filtered back projection (FBP) algorithm. The FBP algorithm is mainly used for radiographic inspection using X-ray [18,19]. Although high resolution is shown in the radiographic inspection, there is a disadvantage that image artifacts are generated when ultrasonic tests are applied. Other works have been based on the reconstruction algorithm for the probabilistic inspection of damage (RAPID) [20–23]. The RAPID algorithm is actively used in ultrasonic tomographic techniques as a technique for imaging defects using a signal difference coefficient. However, the RAPID algorithm has the advantage of being able to visualize faults with small transmission and reception points, but due to some negative influences such as shape factor (factor of influence), there is a limit to quantifying the defects. It is also not suitable for multidefect imaging.

In this study, in order to overcome the limitations of the resolution of the RAPID algorithm, which is typical of the existing ultrasonic tomographic algorithm, the FBP algorithm, an imaging technique used in the radiography technique, was applied to the ultrasonic technique. We confirmed the problem with the image artifacts generated in the FPB algorithm using ultrasonic waves. Difference of the projection data, Hilbert transform of the difference data, distance weight, and back projection were applied to the FBP algorithm to reconstruct the Difference Hilbert Back Projection (DHB) algorithm. The radiographic imaging techniques require many data points and reliable data for high-resolution imaging. However, manual operation is still being widely used for data acquisition. The work efficiency of manual operation is very low, and the precision of signal acquisition cannot be guaranteed. Although automatic control was used in some studies, many of the devices can only be used in some special circumstances. In this work, a laser switch has been adopted in an automatic detection system to improve the precision of signal acquisition. The automatic detection system was developed based on the hybrid application of a pulse laser and an air-coupled transducer. This is one of the best combinations among many different kinds of noncontact NDT methods. The detection system consists of two main parts. One part is an automatic scanning robot arm for the air-coupled transducer. Another part is an automatic clamping device for different kinds of specimens to be tested. The tomography imaging can be conducted efficiently by using this automatic detection system. High-precision signal acquisition can be guaranteed with the help of the laser switch. The iterative reconstruction method used in this work is the fan-beam method. The practicability of this detection system has been confirmed by experimental results. The experiment results matched well with both the theoretical simulation and the actual defects. The imaging quality has been improved to a great extent compared with other methods used in earlier studies.

2. Tomography Theorem

Tomography imaging was used to obtain the section view of the specimen under testing. Image reconstruction from the data projection is a mathematical problem. The original object can be copied from a large number of projection signals. The results of computed tomography are the distribution image of the linear attenuation coefficients.

The DHB algorithm used in this work has evolved from the traditional FBP algorithm. The experiment results show that the imaging quality obtained from the DHB algorithm is much better than that obtained from other analogous algorithms such as RAPID or FBP. These two frequently used algorithms are also discussed to emphasize the advantages of the new DHB algorithm. The theoretical foundation and the corresponding experimental results will be illustrated in the following part of this paper.

The RAPID is based on a damage index known as the signal difference coefficient (SDC). This SDC can be taken as a measurement of how statistically different the defect signals are from a baseline nondefect signal. Damage indexes for all transducer pairs are spatially distributed. Those damage indexes are summed to generate an image of the damage area. The first step of this algorithm is to calculate SDC between the current signal $x_{ij}(t)$ and the reference $y_{ij}(t)$. The index i is for the transmitter and j is for the receiver. Mathematically, the SDC can be stated as:

$$SDC_{ij} = 1 - \left| \frac{\int_{t_0}^{t_0+\Delta T} [x_{ij}(t) - \mu_x][y_{ij}(t) - \mu_y]^2 dt}{\sqrt{\int_{t_0}^{t_0+\Delta T} [x_{ij}(t) - \mu_x]^2 dt \int_{t_0}^{t_0+\Delta T} [y_{ij}(t) - \mu_y]^2 dt}} \right|, \quad (1)$$

where t_0 is the direct arrival time for each transducer pair, μ_x and μ_y are the mean values of the corresponding current signal and baseline signal, and ΔT is the time window. The next step after the SDC values for all sensor pairs are calculated is image reconstruction. An image is generated by distributing each SDC value spatially on the image plane in an elliptical pattern. The two foci of the ellipses are the two transducers' locations. A parameter β controls the size of the ellipse. The amplitude linearly tapers from its maximum value along the line connecting the ellipse foci to zero on the periphery of the ellipse. The parameter β is a shape factor that controls the size of the elliptical distribution. Its value can be arbitrary, but greater than 1.0. Finally, the image amplitude at each pixel is a linear summation of the location probabilities from each transmitter–receiver pair (M). In Equation (2), the coordinate position of the image is displayed. x_{RK}, y_{RK} is the coordinate position of the sensor with x_{RK}, y_{RK} is the coordinate position of the receiving sensor. $P_K(x, y)$ is the image value of image obtained from a pair of sensors and sensors. $P(x, y)$ is the sum of the image values obtained from the sensors of all pairs (M) and the receiving sensor. $R(\mathrm{x}, \mathrm{y}, \mathrm{x}_{TK}, y_{TK}, x_{RK}, y_{RK})$ is a formula showing the relationship between the coordinate position of the image and the position of the sensor. The larger the $R(\mathrm{x}, \mathrm{y}, \mathrm{x}_{TK}, y_{TK}, x_{RK}, y_{RK})$, the farther away from the shortest distance of the pair of sensors. β is a shape factor that limits the coverage of $R(\mathrm{x}, \mathrm{y}, \mathrm{x}_{TK}, y_{TK}, x_{RK}, y_{RK})$.

$$P(x, y) = \sum_{i=1}^{N-1} \mathrm{P}_k(x, y) = \sum_{K=1}^{M} \frac{SDC}{\beta - 1} \{\beta - R(x, y, x_{TK}, \mathrm{y}_{TK}, x_{RK}, y_{RK})\} \quad (2)$$

The RAPID has been widely used in the field of nondestructive testing. However, some disadvantages of this algorithm are gradually being exposed with the increasing demands of imaging quality. Those disadvantages are listed as follows. In signal extraction, the time window ΔT in Equation (1) should cover at least two modes of Lamb waves because it is necessary to know the difference between the current signal and baseline signal. A smaller correlation coefficient value means a stronger indication of the defect's appearance. This will undoubtedly make the guided wave tomographic imaging become more complex. Particularly, this adverse effect will become more serious when the air-coupled transducer is used because air-coupled transducers are insensitive to the symmetric modes of a Lamb wave. On the other hand, only one mode of the Lamb wave is needed if the DHB algorithm is used. In defect quantitative analysis, the parameter β determines the shape of the elliptical path. Then, the speckle of the defect shape can also be influenced. There is one optimal value for specific defects with a determined size. Other defects of different sizes cannot be imaged successfully. The influence of β on the imaging results is shown in Figure 1.

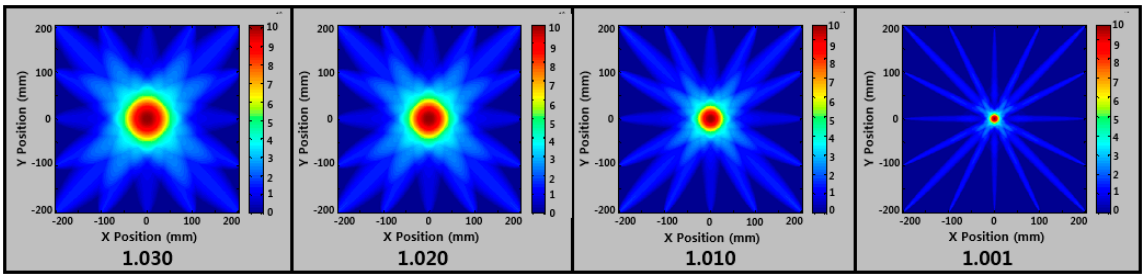

Figure 1. Image reconstruction results by using different values of parameter β.

The FBP algorithm is also widely used in the NDT field. Its reconstruction formula can be written as:

$$f(\vec{x}) = \int_0^{2\pi} \frac{D}{(D + \vec{x} \cdot \vec{e}_w)^2} \int_{-\gamma_m}^{\gamma_m} (q(\lambda, \gamma) \cos \gamma) \otimes h_H(\gamma) d\gamma d\lambda, \quad (3)$$

where $\vec{x}$ is the vector of the reconstruction points, λ is the angle between the starting coordinate axis and the line that connects the trigger points and the origin of the starting coordinate system, λ_m is the angle range of the fan beam, $q(\lambda, \gamma)$ is the projection value, $\vec{e}_w$ is unit orthogonal vector, h_H is kernel of the Hilbert transform, and D is the distance between the trigger points and the intermediate point of the receiving sensors' array.

Many different kinds of iterative reconstruction methods can be used for the data acquisition, as shown in Figure 2. Only the fan-beam method was used in this work to emphasize the comparison of the imaging quality of different tomographic imaging algorithms.

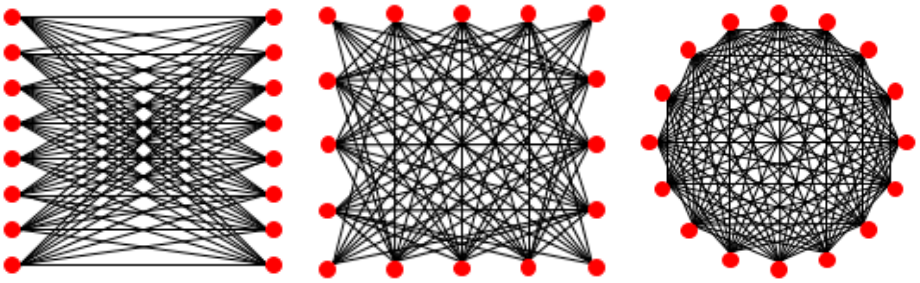

Figure 2. Three common iterative reconstruction methods: (**a**) Crosshole; (**b**) Double-crosshole; (**c**) Fan-beam.

As shown in Figure 3, it is based on the signal of a nondefective ultrasonic signals, and the nondefective signal becomes a reference signal. When the ultrasonic wave passes through the defect, the ultrasonic amplitude is attenuated, so the defect or object is imaged by utilizing the difference in amplitude between the two signals. The simulated results were made based on the attenuation law of a Lamb wave. As shown in Figure 4, results based on different detection points were made for comparison. The FBP algorithm is a technique used in radiographic inspection. It is a method of transmitting X-rays through an object and receiving it through a detector. It shoots 360 degrees around the object and displays the image. However, radiographic inspection is limited by shielding facilities or radiation regulations. In this study, ultrasonic technology using a Lamb wave was applied to compensate for such shortcomings. Figure 4 is the result of imaging by applying the simulation signal of Figure 3 to the FBP algorithm. The imaging quality can be improved by increasing the emitter and receive detection points. This method has the same characteristic as the new DHB algorithm in this respect. The number of the detection points adopted in the actual experiment was 90, 120, and 180.

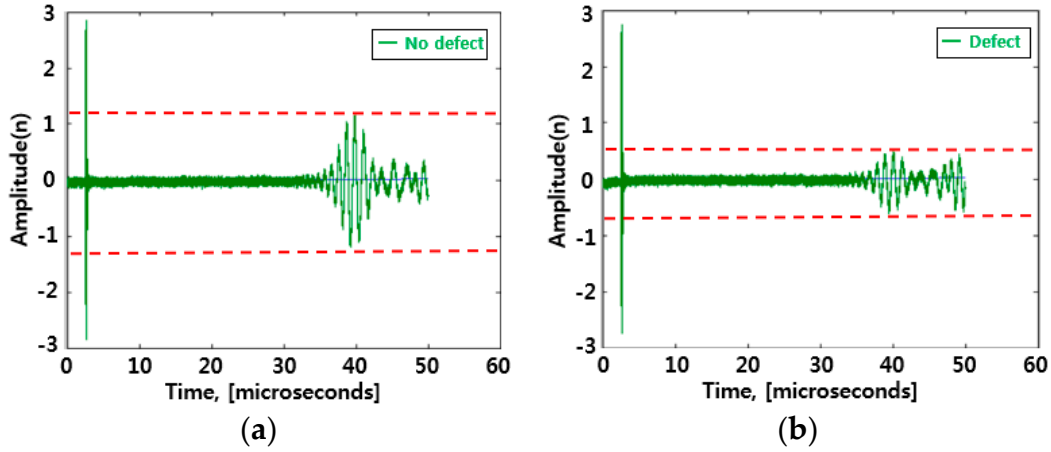

Figure 3. Guided wave signal: (**a**) No defect signal; (**b**) Defect signal.

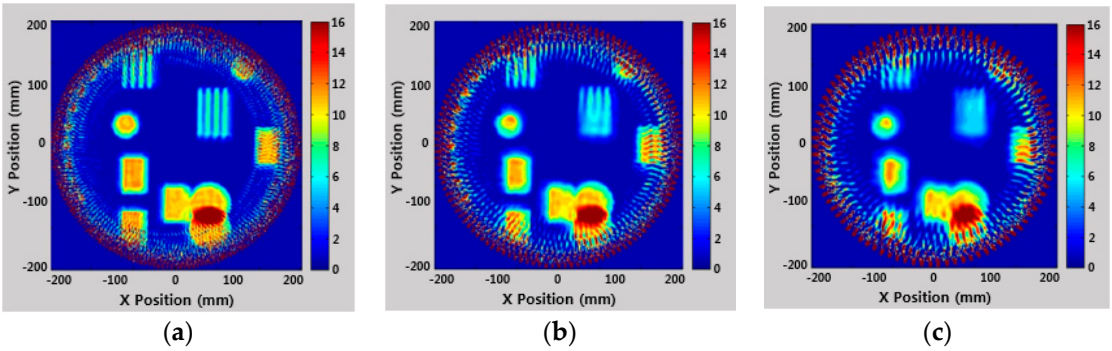

Figure 4. Simulated results from the filtered back projection (FBP) algorithm: (**a**) 180 Points; (**b**) 120 Points; (**c**) 90 Points.

The FBP algorithm has a big advantage in the aspect of imaging precision compared with RAPID. However, the problem of this algorithm is in its image artifacts. Defect imaging close to the scanning edge cannot be displayed clearly, as shown in Figure 4. These are called image artifacts. The image artifacts will undoubtedly affect the precise identification of the defects near the detection boundary.

The new DHB algorithm is proposed to solve the shortcomings of the algorithms discussed above. The new DHB algorithm has good performance in the detection of plate-like structures. The imaging quality can be significantly improved compared with other algorithms, such as RAPID or FBP. Particularly, it can give accurate size and shape of different kinds of defects.

The geometry of the corresponding fan-beam iterative reconstruction method is shown in Figure 5. Its reconstruction formula is Equation (4) [24]. The relevant parameters in Equation (4) are the same as in Equation (3). The unit orthogonal vector $\vec{e}_w$ is represented by $\vec{a}(\lambda)/\|\vec{a}(\lambda)\|$ and is substituted into Equation (3). The notation $g_m(\lambda,\gamma)$ is used to denote the measured projections. Three steps are included in using this method: the difference of the projection data, the Hilbert transform of the difference data, the distance weight, and back projection. The corresponding geometry schematic can be referenced in Figure 5.

$$f(\vec{x}) = \frac{1}{4\pi}\int_0^{2\pi} d\lambda \frac{D}{\|\vec{x}+\vec{\alpha}(\lambda)\|}\int_{-\gamma_m}^{\gamma_m} d\gamma h_H \sin(\gamma'-\gamma)\left(\frac{\partial}{\partial\lambda}+\frac{\partial}{\partial\gamma}\right)g_m(\lambda,\gamma). \quad (4)$$

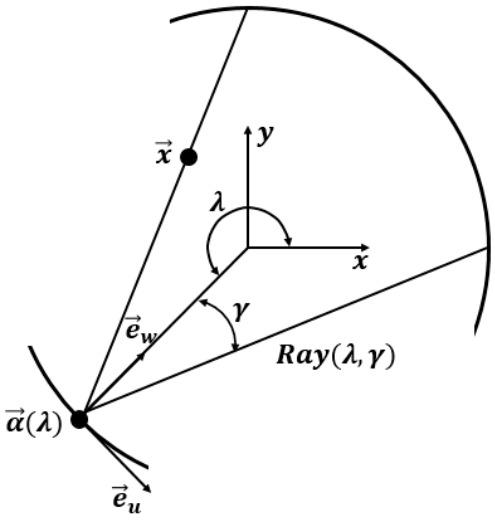

Figure 5. Fan-beam geometry based on the equiangular rays.

The same simulated results have been made by using the DHB algorithm. As shown in Figure 6, the problem of image artifacts can be solved perfectly. The imaging quality is also improved to a large extent.

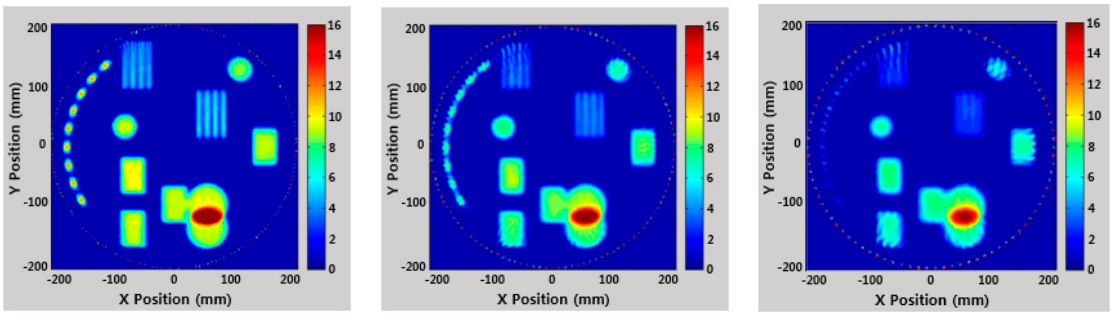

(**a**) (**b**) (**c**)

Figure 6. Simulated result from the Difference Hilbert Back Projection (DHB) algorithm: (**a**) 180 Point; (**b**) 120 Point; (**c**) 90 Point.

In addition, short-scan conditions can also be relaxed once the new DHB algorithm is used. It is generally believed that accurate and stable reconstruction of any region of interest (ROI) requires line integrals of the object density for all lines passing through the object. This condition leads to the notion of circular short scan. As shown in Figure 7, $\pi + \theta$ is referred to as a short scan.

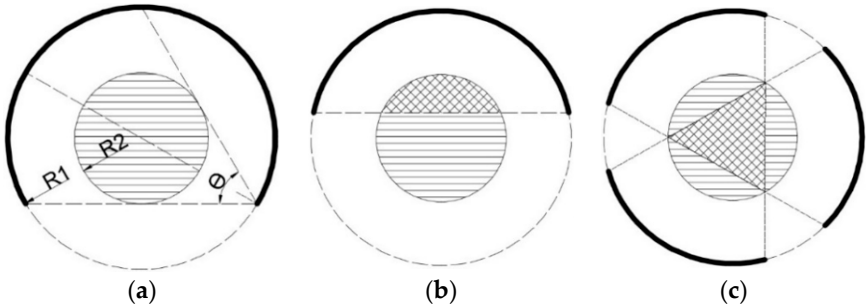

(**a**) (**b**) (**c**)

Figure 7. Schematic of the short-scan problem: (**a**) A conventional short-scan of $\pi + \theta$ allows reconstruction of the whole object; (**b**) A continuous scan of less than $\pi + \theta$ allows reconstruction of all object points inside the convex hull of the scan; (**c**) A scan of three equally spaced segments of 80° each allows reconstruction of a triangular ROI in the center of the object.

All line integral measurements through the object are required for any ROI reconstruction using the conventional FBP algorithm. However, this problem can be relaxed using the new DHB algorithm. As shown in Figure 7c, small central ROIs can be reconstructed using several short arcs if only an ROI inside the object needs to be reconstructed. Reconstruction is possible for any ROI inside the central triangular region obtained by joining the beginning point of each arc with the end point of the next arc.

3. Experimental Set-Up and Specimen

The hybrid application of an air-coupled transducer and pulse laser is used in this work. Air-coupled sensors can have increased sensitivities compared to optical transducers. Well-designed capacitive air transducers can be expected to be as sensitive as laser interferometric sensors [25,26]. In addition, the air-coupled transducers can receive a specific mode of guided waves. This can be realized by changing the receiving angle to a leak direction of the selected modes. It is well-known that a static scanning process of the receiver is very important for high-precision acquisition of the signals. The application of air-coupled transducers is one of the most appropriate choices to realize high-precision acquisition. However, the mismatch of acoustic impedances between solid materials and air is a huge weakness of a purely air-coupled transducer detection system. Consider the scenario shown in Figure 8. The ultrasound passes through the interface between the solid specimen and air two times. Only a tiny fraction (10^{-8}) of the original acoustic energy is transmitted through both solid–air interfaces to reach the receiver.

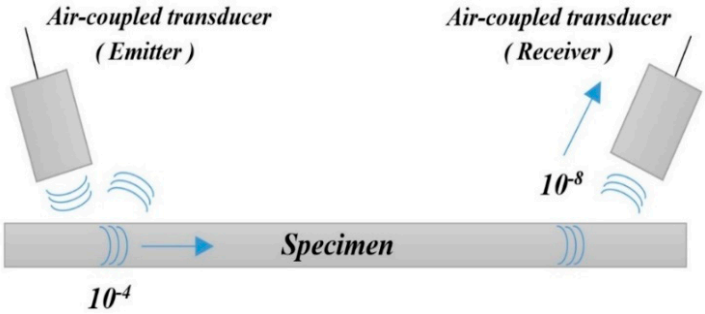

Figure 8. Transmission in air using two air-coupled transducers. Values shown are approximate fractions of the original energy.

Consider the second scenario shown in Figure 9. The ultrasound is generated directly in the solid using a pulsed laser. The solid–air interface on the generation part has effectively been removed. The energy reaching the receiver could increase by a factor of 10^4 [27]. As a receiver, the air-coupled transducer can also have good performance if the proper parameters are set [28]. The hybrid application of an air-coupled transducer and pulse laser can make material characterization more feasible. It can also be used where the air-coupled transducer and pulse laser are put on the opposite sides of the specimen [29,30]. The laser ultrasonic technique can also be used in the detection of a curved surface specimen [31,32].

A line laser source is much better than a point source for long-range detection [33,34]. Many researchers used spatial array illumination sources produced by several means. Those methods include slit masks, lenticular arrays, optical diffraction gratings, multiple lasers, and interference patterns. The linear slit array mask was used in this study, as shown in Figure 10. A Lamb wave of specific modes can be generated selectively by adjusting the line spacing. The distance between two adjacent line laser sources is defined as the line spacing or element gap marked as ΔS. The value of the line spacing is equal to the wavelength of the generated Lamb wave. The difference between it and the element width equals the width of the single line laser source. The width of the single line light source is also known as the line width marked as w. The value of $w/\Delta s$ is known as the duty ratio. It is found that an A0 mode Lamb wave has the optimum signal–noise ratio when the value of $w/\Delta s$ is 0.5 [35].

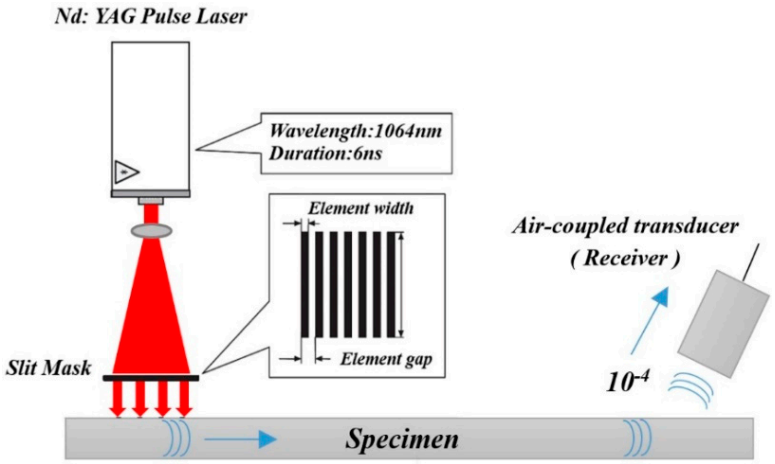

Figure 9. Improved transmission using a laser source. Values shown are approximate fractions of the original energy.

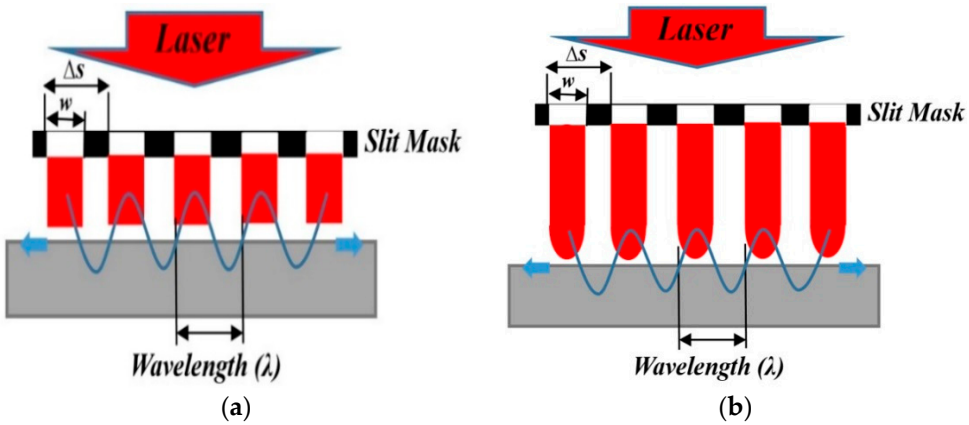

Figure 10. Schematic of the line laser sources of 1-D and Gaussian model: (**a**) One-dimensional theory; (**b**) Gaussian model.

As shown in Figure 10b, the generated wave should be analyzed by using a Gaussian model. Specifically, the spatial energy profile of each line beam is assumed as Gaussian. A Gaussian model is also suitable for the focused laser beams. However, the diffraction effect is negligible when the slit mask is very close to the target surface. Then, the spatial energy profile of each line beam is closer to a square pulse than Gaussian in the line-arrayed slit mask shown in Figure 10a. The energy of each line laser beam can be assumed to have a uniform distribution, and the temporal profile is a delta function. The spatial energy profile of each line beam can be taken as a simple one-dimensional square pulse. For an array of N equally spaced identical laser sources, the final displacement can be taken as a summation of N single-source surface waves displaced in time by the surface wave propagation interval between two adjacent sources, as shown in Equation (5).

$$g(t) = \sum_{n=1}^{N} f(t - n\Delta t) \tag{5}$$

In the above equation, $\Delta t = \Delta s/c$ and $f(t)$ is the out-of-plane displacement of the guided wave generated by a single line laser source. It is expressed as a function of time in the thermoelastic regime. The displacement is proportional to the derivative of the absorbed laser energy function. The energy distribution of the line laser beams was regarded as a square pulse, and $f(t)$ can be approximated by

the square pulse derivative. The relationship between the Lamb wave frequency dispersion curve and the corresponding parameters is given in Figure 11.

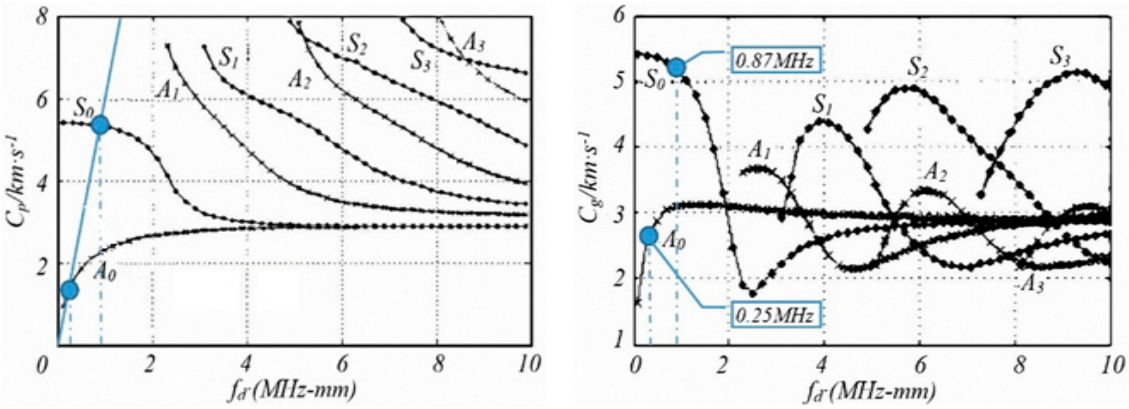

(**a**) (**b**)

Figure 11. The frequency dispersion curve of a Lamb wave and the corresponding parameters: (**a**) Phased velocity; (**b**) Group velocity.

The signal is generated on the specimen surface when the illuminated laser beam transmits through the slit mask. The wavelength corresponds to the element gap of the slit array. The relation between the wavelength, phase velocity, and wave frequency is shown in Equation (6), where d is the specimen thickness, f is frequency, and λ is wavelength. The principle of generating the desired mode is shown in Figure 11.

$$C_{ph} = f \cdot \lambda = f \cdot \Delta s = f \cdot d \cdot \left(\frac{\Delta s}{d} \right). \quad (6)$$

As shown in Figure 11, a diagonal line with a slope of $\Delta s/d$ is described in the dispersion curves of the Lamb wave. The modes of the curves that have cross points with the diagonal line can be generated. Therefore, various modes with different frequencies can be generated simultaneously.

The experimental setup is shown in Figure 12. A Nd:YAG pulsed laser with a wavelength of 1064 nm and a pulse duration of 6 ns was used as the energy source. A Quantel Brilliant B pulsed YAG laser was used with principal radiation at 1064 nm, max energy/pulse 850 mJ, max average power 7.5 W, and pulse duration 6 ns. This laser beam was expanded and illuminated on a slit mask. The slit mask is located close to the specimen surface to suppress the diffraction phenomena.

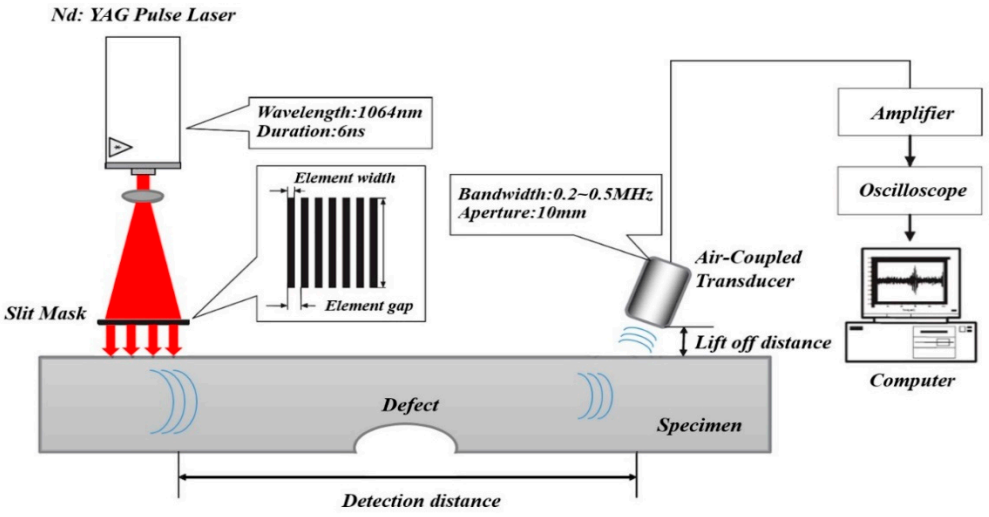

Figure 12. Schematic diagram of the experimental setup.

An unfocused planar air-coupled transducer with a circular aperture was used as the receiver. It was placed on an automatic scanning robot arm. The diameter of its aperture area is 10 mm. The air-coupled transducer used in the experiment is a transducer capable of transmitting and receiving broadcast frequencies. It can detect an ultrasonic wave in air with a frequency range of 0.2 to 0.5 MHz. The lift-off distance of this air-coupled transducer from the specimen surface is 7 mm. The air-coupled transducer has a small amplitude because it receives ultrasonic waves through the air noncontacting the specimen. Therefore, an amplifier is used to amplify the signal. There are two key points that contribute to the imaging quality of the tomography. One is the algorithm, and another one is the high-accuracy acquisition of signals. By using the automatic scanning robot arm, the air-coupled transducer can be positioned automatically with the right receiving angle. The details of the automatic position will be illustrated. The wave propagation direction and the receiving direction of the air-coupled transducer should be kept in the same straight line in practical application. Although the line source is based on a one-dimensional model, the pulse laser has a Gaussian model [36]. This makes the accurate positioning of the air-coupled transducer very important. Thus, an automatic positioning robot arm was developed in this work.

Figure 13 shows the characteristics of the Gaussian beam. In the wave traveling toward the focus $(z = 0)$, the beam width is continuously reduced, so that the beam width is minimized at the focus. Wave past focus increases beam width almost linearly. Suppose that the electromagnetic wave is traveling in the +z direction, and also assume that the Gaussian beam changes like a Gaussian function in the x and y axis directions perpendicular to the z axis. Then, Equation (7) can be obtained.

$$E(\bar{r}) = A(z)\exp\left[i\frac{k\rho^2}{2q(z)}\right]\cdot e^{ikz}, \text{where } \rho^2 = x^2 + y^2 \tag{7}$$

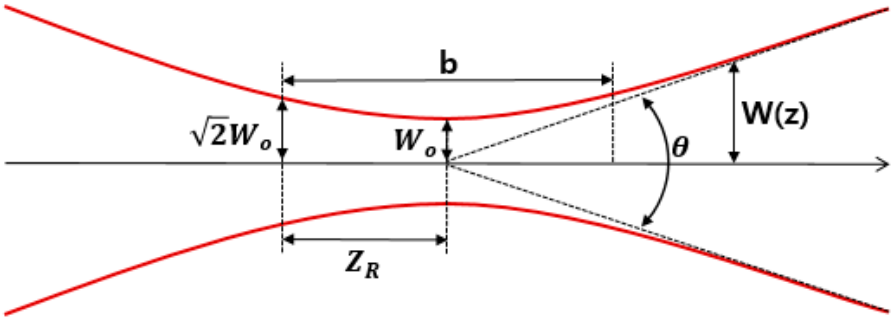

Figure 13. Gaussian beam propagation factor.

Here, K is the wave number, and the gauss beam moves in the +z direction, so the beam width widens and the phase changes, so if $q(z)$ in Equation (8) is defined as plural, Z_R can be defined by considering Figure 13. Referring to Figure 13, W_o has the smallest beam width $(z = 0)$, so measurement is possible. That is, since Wo is half the beam width, Z_R is also determined by $W(z)$. Z_R is called Rayleigh length, and $W(z)$ is increased by $\sqrt{2}$ times at $Z = Z_R$, and the position of $Z = Z_R$, which is doubled by the area of the beam, becomes Rayleigh length.

$$\left|A(z)\right| = \sqrt{2\eta P_0}\sqrt{\frac{2}{\pi}}\frac{1}{w(z)} \tag{8}$$

Even if the Gaussian beam travels in the +z direction, the total power must not change, so $A(z)$ can be expressed as Equation (8). Substituting 2 into Equation (7), the Gaussian beam formula is

defined as Equation (9). By installing the lens using the formula, a plane wave is generated through the lens, and when passing through the slit, a desired wave can be created.

$$E(\bar{r}) = E_0 \sqrt{\frac{2}{\pi}} \frac{w_0}{w(z)} \exp\left[-\frac{\rho^2}{w^2(z)} + i\frac{k\rho^2}{2R(z)}\right] \cdot e^{ikz} \quad (9)$$

As shown in Figure 14, the scanning process consisted of four steps, and the initial condition is given in step 1. The air-coupled transducer should firstly revolve at a certain angle α around the test center when it is necessary to change the detection points. Then, the slit mask is rotated to make the wave propagation direction stay in the same straight line with the new receiving angle. This process can be very complicated with manual computation and operation. Thus, automatic control was adopted in this work. The LED laser line sources and photoresistors were installed on the edge of the slit mask and the rotation center of the air-coupled transducer. They were marked as $LED_{1/2}$ and $R_{1/2}$, respectively. All the automatic movement in this work is based on a step motor. To rotate the slit mask, LED_1 will be turned on at the same time as the step motor M_1. The illumination direction of LED_1 is the same as that of the wave propagation. The step motor M_1 will stop by itself once the light of LED_1 points to the photoresistor R_1. Then, LED_2 will turn on together with M_2, and the step motor M_2 will also stop automatically once the light of LED_2 points to the photoresistor R_2. The new detection point can be fixed with the right receiving angle automatically based on the process discussed above. The complex calculations and manual operation can be omitted.

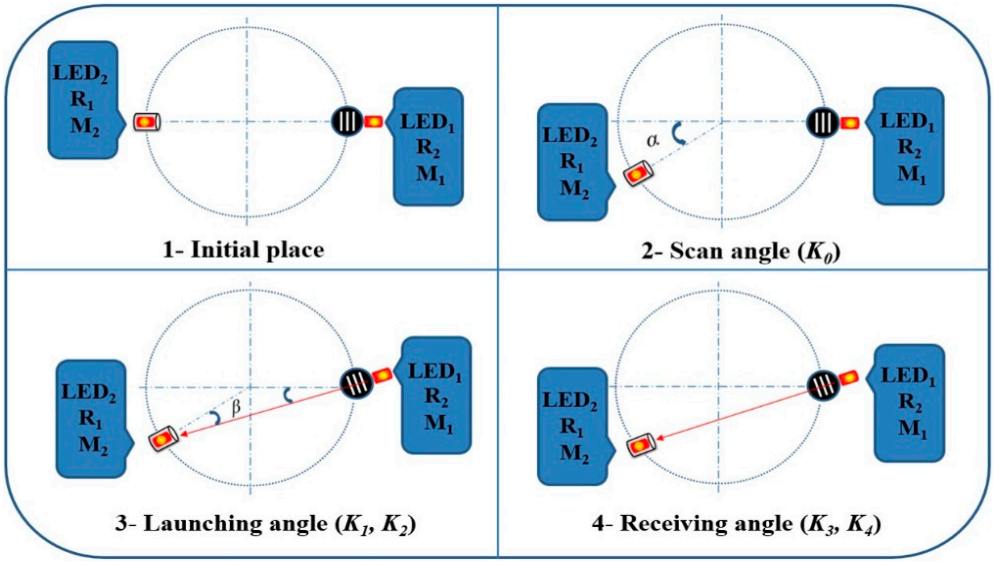

Figure 14. Schematic of the automatic scanning robot arm.

The design of the automatic scanning is shown in Figure 15. The key part here is the photoresistor. Its electrical resistance will decrease immediately if it is illuminated by the light of the laser LED. Then, the corresponding circuit that was used to control the step motor will close. Conversely, the circuit will turn off. In this work, a single chip computer was used to control the step motor. The step motor will be fixed by its magnetic pole once the circuit is controlled by the photoresistor. It can guarantee that the experimental equipment will never be influenced by potential factors from outside. In other words, the movement of the transducer can only be controlled by a program. Then, the detection points can be positioned with very high accuracy with the right receiving angle of the air-coupled transducer.

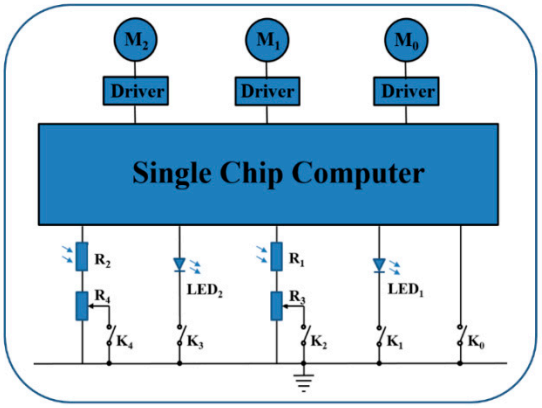

Figure 15. The working principle of the automatic scanning robot arm.

In a practical environment, the photoresistor can also be influenced by sunlight or the bulbs in the lab. Those negative factors can influence the normal operation of the photoresistor, as shown in Figure 16. Adjustable resistors R_3 and R_4 were installed in series with the photoresistors to avoid these influences. They can improve the adaptability of the equipment in different working environments. The photoresistor will only respond to the laser LED by using the method mentioned above. Both the air-coupled transducer and the pulse laser are on the same side of the specimen in the experimental setup. The automatic clamping device will be put on the other side of the specimen. The accurate collection of the signals cannot only rely on the automatic positioning of the air-coupled transducer. The precise movement and fixation of the specimen are equally as important as they are for the air-coupled transducer. Accurate collection can be achieved by using an automatic clamping robot. As shown in Figure 17, it can clamp different kinds of specimens automatically by using four robot arms. The specimens include plates, curved plates, or even pipes. There are four lead-screw mechanisms that are used to control the robot arms. Those robot arms can stop by themselves once they come into contact with the specimen boundaries. The movement of those robot arms will never be influenced due to the self-locking phenomenon of the lead-screw mechanisms.

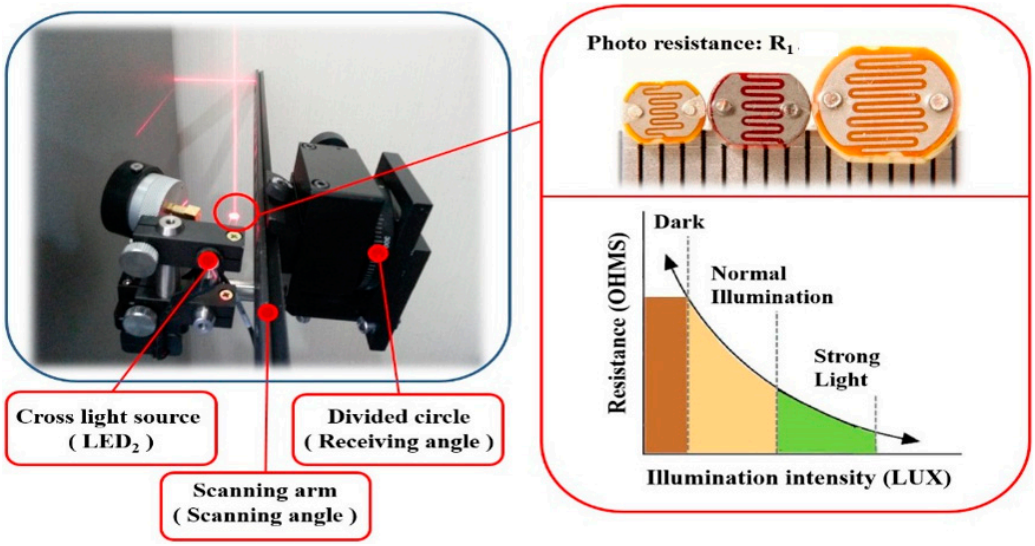

Figure 16. The actual settings of the automatic scanning robot arm.

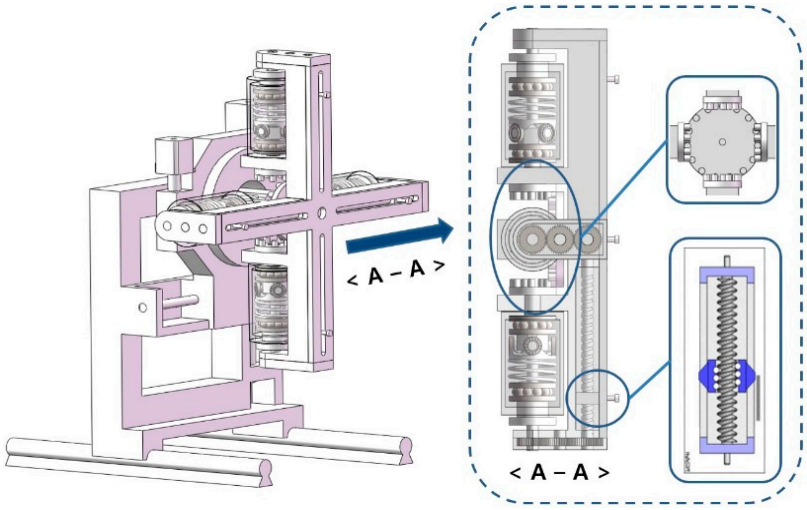

Figure 17. The 3-D model of the automatic clamping robot arms.

The key part of the automatic clamping robot arm is an automatic clutch. The robot arm can clamp the plate specimen with different shapes automatically by using this part, and the clamping force is adjustable. As shown in Figure 18, two transmission shafts are connected together based on elastic force. Those two shafts will always be connected if F_p is not bigger than a maximum value. Otherwise, no force can be transferred through this mechanism. The corresponding calculation formulas are shown in Equations (10) and (11).

$$F_p = F_e < F'_e \tag{10}$$

$$F'_p = F'_e = -k \cdot x \tag{11}$$

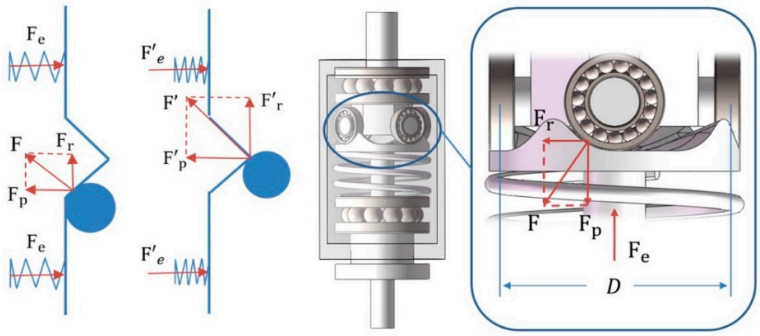

Figure 18. The force analysis of the automatic clutch.

Each of the four robot arms can stop by itself if it comes into contact with the specimen's boundaries. At the same time, the other robot arms will continue to clamp the specimen until they also come into contact with the specimen's boundaries.

In this work, all of the linear motion is based on the lead screw mechanisms, and all of the circular motion is based on worm and gear mechanisms. A self-locking effect can be realized by using both mechanisms. The reliability of the necessary movement in actual operation can be guaranteed in a further step based on the self-locking effect. The actual experimental platform is shown in Figure 19. The air-coupled transducer was placed on the same side of the specimen together with the pulse laser. The clamping robot arms was fixed on the other side of the specimen. The clamping robot arms were installed on a scanning device through which high-accuracy positioning of the specimen can be achieved.

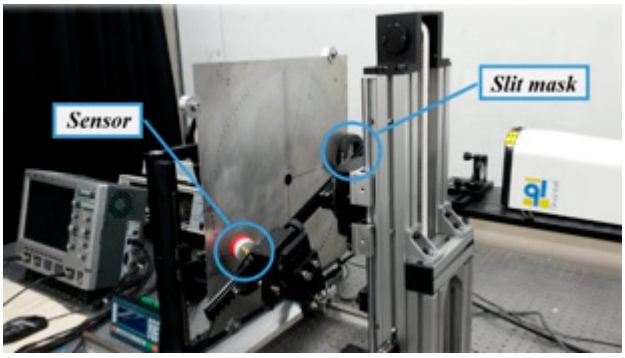

Figure 19. The actual experimental platform.

4. Results and Discussion

In this work, the test specimen is an aluminum plate with a thickness of 1 mm. The wavelength was designed as 6 mm. Both the A_0 and S_0 modes of a Lamb wave can be excited based on the laser ultrasonic technique. Because the air-coupled transducer is more sensitive to the antisymmetric modes than the symmetric modes, the detection range of the air-coupled transducer was chosen as 0.2 to 0.5 MHz to detect the A_0 mode Lamb wave.

An experiment was done to see the appearance of a defect, as shown in Figure 20. There is a penetrating hole in the center of the specimen. The diameter of this through hole is 20 mm.

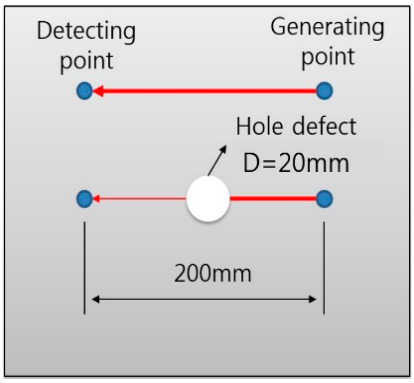

Figure 20. The schematic of the defect-detecting experiment.

The signal of both the defect-free and with the defect areas have been obtained in both time and frequency domains. As shown in Figure 21, the signal attenuates clearly due to the appearance of the defect. Only an A_0 mode Lamb wave can be detected, as mentioned above. The generated S_0 mode was filtered by the air-coupled transducer due to its detection range. Only one mode of the Lamb wave was needed for the tomography once the new DHB method was used. This is also another advantage of the new algorithm. For example, the probabilistic algorithm requires at least two modes of Lamb waves for comparison. The tomographic imaging technique used in this work is based on the wave attenuation. The attenuation law of a Lamb wave is subject to Equation (12), and the equation for data projection is given in Equation (13). The parameter α in those two equations is the attenuation coefficient, A is the signal amplitude, and x is the propagation distance.

$$A = A_0 e^{-\alpha x} \tag{12}$$

$$\int_{-\infty}^{\infty} \alpha(x)dx = \ln \frac{A_0}{A} \tag{13}$$

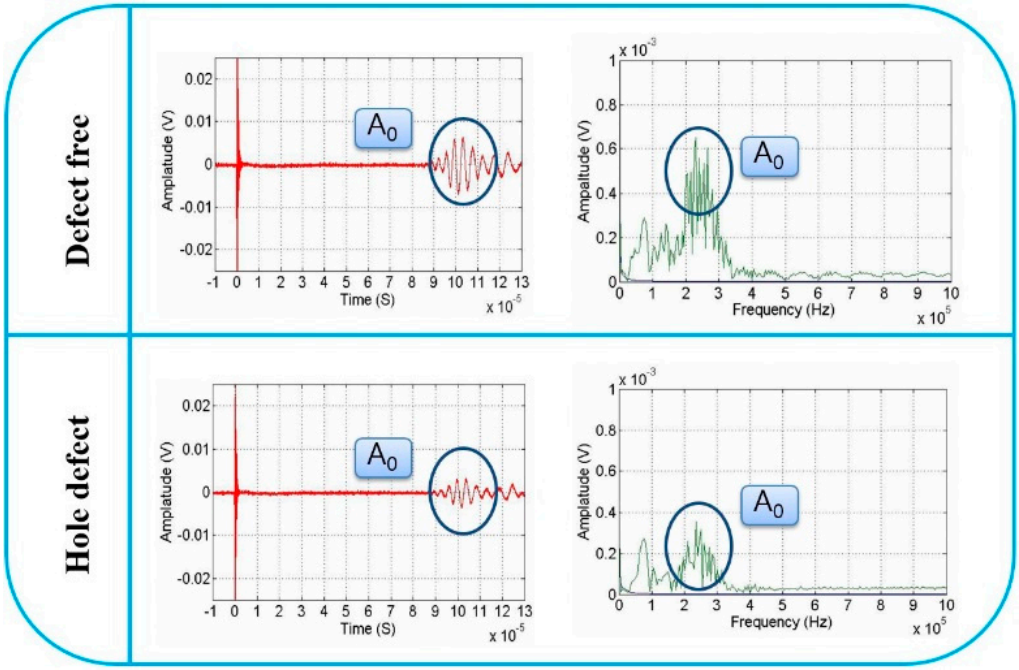

Figure 21. The signals of the defect detecting experiment.

The attenuation curve and the corresponding scanning sketch based on the fan-beam iterative method are shown in Figure 22a,b. The signal attenuation becomes evident within the scanning range of 83° to 90° in the area where a defect starts to appear. Particularly, the illumination area can cause a "dead zone" due to the geometrical features (the diameter of the slit mask used in this work is 60 mm). In other words, the detection cannot be achieved effectively along a full circle arc when the line laser source is used. As shown in Figure 22, the signal within the scanning range of 0° to 13° was invalid data.

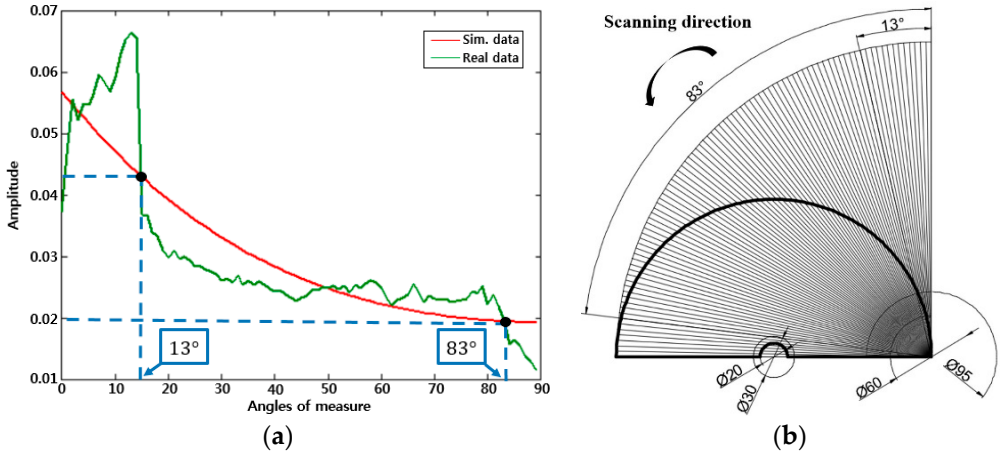

(**a**) (**b**)

Figure 22. The attenuation curve of Lamb wave obtained from the experiment: (**a**) Attenuation curve; (**b**) Schematic of scanning direction.

It is unnecessary to test the "dead zone" when the DHB algorithm is used because the short-scan condition can be relaxed to a great extent. The real data shown in Figure 22 also supports the advantage of this new DHB algorithm compared with FBP or other algorithms. Figure 23a,b is a sample drawing and specimen of the initial single defect. The imaging of the penetrating hole is given in Figure 24. There are 36 emitter and receive points. If there are 19 receiving points from a single emitter point to a semicircle, and inspection is performed up to the 20th emitter point, 361 data points can be collected.

Complex shapes or multiple defects should be inspected up to the 36th emitter point, but a single circular defect, as shown in Figure 24, was able to quantitatively represent the defect. The imaging of the defect is displayed clearly compared with the defect-free area.

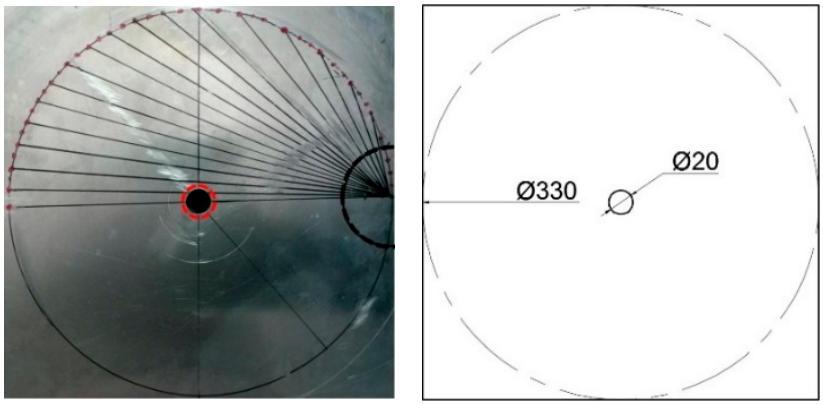

Figure 23. Circular defect specimen #1: (**a**) Circular defect specimen; (**b**) Circular defect specimen drawing (Unit: mm).

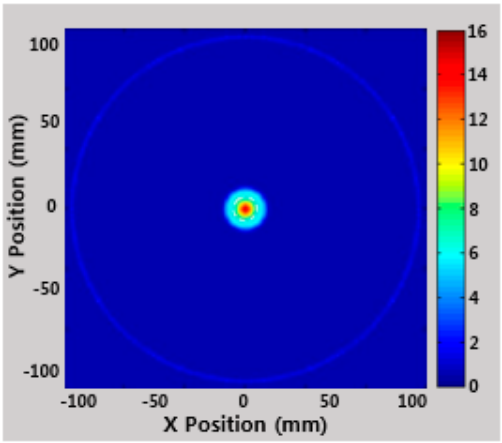

Figure 24. Circular defect imaging.

Another experiment was conducted to further verify the effectiveness of the new DHB algorithm in the aspect of detection precision. Different types of defects were made in different positions of specimen #2. As shown in Figure 25, the defects include 10 micropores, one narrow through defect (width 2 mm, length 52 mm), and two nonpenetrating defects (circle defect: diameter 52 mm, depth 0.5 mm) (rectangular defect: width 52 mm, length 26 mm, depth 0.2 mm) with different depth, which can be considered as an imitation of corrosion defects. There are 106 emitter and receiver points. If there are 53 receiving points from a single emitter point to a semicircle, and inspection is performed up to the 106th emitter point, 5618 data points can be collected. Specimen #2 has multiple defects in various shapes, so the more imitators and reception points, the more quantitatively the defects can be represented. Although it has so many emitters and receiving points, it was able to receive uniform data through the robot arm. Figure 26 shows the imaging results of specimen #2. The imaging results agree very well with the actual defects.

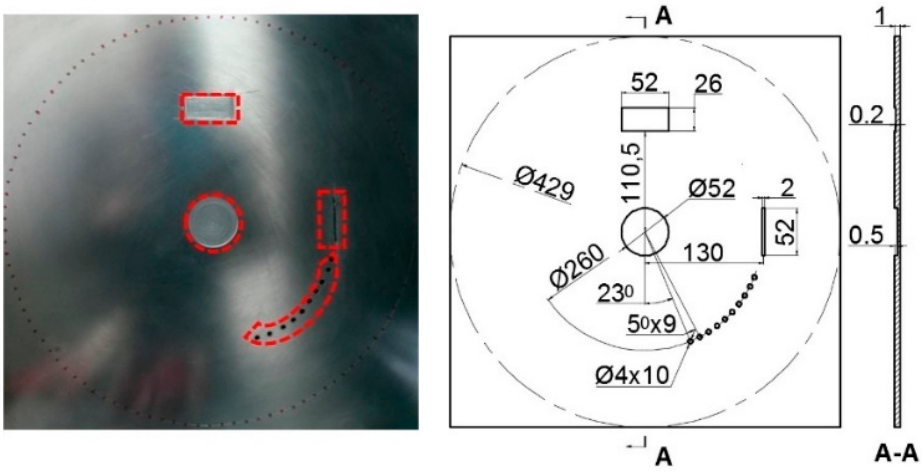

(**a**) (**b**)

Figure 25. Image reconstruction of specimen #2: (**a**) Multidefect specimen; (**b**) Multidefect specimen drawing (Unit: mm).

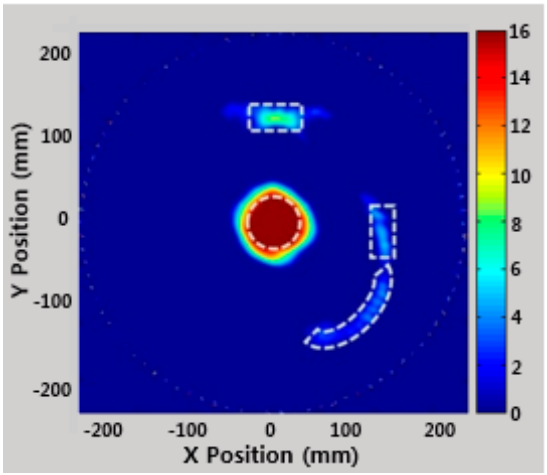

Figure 26. Multidefect imaging using the DHB algorithm.

5. Conclusions

The hybrid application of an air-coupled transducer and pulse laser has been adopted in this paper. The FBP algorithm, which is mainly used in radiographic inspection, was applied to ultrasonic testing and tomographic imaging, and the disadvantages of image artifacts were confirmed. The factors affecting image quality, such as image artifacts, were overcome with the DHB algorithm through three projection data processing steps; Hilbert transform of the difference data, distance weight, and back projection. A new DHB algorithm has been successfully applied to give accurate imaging of different kinds of defects in plate-like structures. The imaging results agree very well with the actual defects. Particularly, the detection efficiency has been improved to a large extent by using the automatic scanning system. Further research will focus on the detection of different kinds of specimens with different geometries, such as curved surfaces. The algorithm should be further improved to make high-quality images with fewer detection points. The presented techniques can be applied to structural health monitoring to predict faults by quantitatively imaging the growth status of the faults.

Author Contributions: J.P. and Z.L. designed and performed the experiments. Y.C. conceived the original idea. J.P. developed the theory and performed the computations with support from J.L. and Y.C. verified the analytical methods. J.L. and Z.L. wrote the draft paper, J.P. completed the final paper, and Y.C. made the final review. All authors have read and agreed to the published version of the manuscript.

Funding: This work was supported by National Research Foundation of Korea (NRF) grant funded by Korea government (MSIT)(NRF-2020M2D2A1A02069933).

Acknowledgments: Authors appreciate the support from Wang Yu at University of Electronic Science and Technology of China.

Conflicts of Interest: The authors declare no conflict of interest.

References

1. Jansen, D.; Hutchins, D.A. Immersion tomography using Rayleigh and Lamb waves. *Ultrasonics* **1992**, *30*, 245–254. [CrossRef]
2. Hutchins, D.A.; Jansen, D.P.; Edwards, C. Non-contact Lamb wave tomography using laser-generated ultrasound. In Proceedings of the IEEE Ultrasonics Symposium, Tucson, AZ, USA, 20–23 October 1992; Volume 2, pp. 883–886.
3. Hutchins, D.A.; Jansen, D.; Edwards, C. Lamb-wave tomography using non-contact transduction. *Ultrasonics* **1993**, *31*, 97–103. [CrossRef]
4. Ho, K.S.; Billson, D.R.; Hutchins, D.A. Ultrasonic Lamb wave tomography using scanned EMATs and wavelet processing. *Nondestruct. Test. Eval.* **2007**, *22*, 19–34. [CrossRef]
5. McKeon, J.C.P.; Hinders, M.K. Parallel projection and crosshole Lamb wave contact scanning tomography. *J. Acoust. Soc. Am.* **1999**, *106*, 2568–2577. [CrossRef]
6. Li, W.; Cho, Y. Combination of nonlinear ultrasonics and guided wave tomography for imaging the micro-defects. *Ultrasonics* **2016**, *65*, 87–95. [CrossRef]
7. Lee, J.; Sheen, B.; Cho, Y. Multi-defect tomographic imaging with a variable shape factor for the RAPID algorithm. *J. Vis.* **2015**, *19*, 393–402. [CrossRef]
8. Lee, J.; Sheen, B.; Cho, Y. Quantitative tomographic visualization for irregular shape defects by guided wave long range inspection. *Int. J. Precis. Eng. Manuf.* **2015**, *16*, 1949–1954. [CrossRef]
9. Park, J.; Cho, Y. A study on guided wave tomographic imaging for defects on a curved structure. *J. Vis.* **2019**, *22*, 1081–1092. [CrossRef]
10. Wright, W.; Hutchins, D.A.; Jansen, D.; Schindel, D. Air-coupled Lamb wave tomography. *IEEE Trans. Ultrason. Ferroelectr. Freq. Control.* **1997**, *44*, 53–59. [CrossRef]
11. Liu, Z.; Yu, H.; Fan, J.; Hu, Y.; Cunfu, H.; Wu, B. Baseline-free delamination inspection in composite plates by synthesizing non-contact air-coupled Lamb wave scan method and virtual time reversal algorithm. *Smart Mater. Struct.* **2015**, *24*, 045014. [CrossRef]
12. Rymantas, J.K.; Almantas, V.; Sustina, S. Application of air-coupled ultrasonic arrays for excitation of a slow antisymmetric lamb wave. *Sensors* **2018**, *18*, 2636.
13. Zhao, X.; Royer, R.L.; Owens, S.E.; Rose, J.L. Ultrasonic Lamb wave tomography in structural health monitoring. *Smart Mater. Struct.* **2011**, *20*, 105002. [CrossRef]
14. Rymantas, J.K.; Reimondas, S.; Justina, S. Application of PMN-32PT piezoelectric crystals for novel air-coupled ultrasonic transducers. *Phys. Procedia* **2015**, *70*, 869–900.
15. Rymantas, J.K.; Reimondas, S.; Justina, S. Air-coupled ultrasonic receivers with high electromechanical coupling PMN-32% PT strip-like piezoelectric elements. *Sensors* **2017**, *17*, 2365.
16. Albiruni, F.; Cho, Y.; Lee, J.-H.; Ahn, B.-Y. Non-Contact Guided Waves Tomographic Imaging of Plate-Like Structures Using a Probabilistic Algorithm. *Mater. Trans.* **2012**, *53*, 330–336. [CrossRef]
17. Park, J.; Lim, J.; Cho, Y. Guided-Wave Tomographic Imaging of Plate Defects by Laser-Based Ultrasonic Techniques. *J. Korean Soc. Nondestruct. Test.* **2014**, *34*, 435–440. [CrossRef]
18. Qi, Z.; Chen, G.-H. Direct Fan-Beam Reconstruction Algorithm via Filtered Backprojection for Differential Phase-Contrast Computed Tomography. *X-ray Opt. Instrum.* **2008**, *2008*, 835172. [CrossRef]
19. Bernal, J.; Sanchez, J. Use of Filtered Back-Projection Methods to Improve CT Image Reconstruction. Available online: http://www.researchagate.net/publication/265811375 (accessed on 4 May 2020).
20. Hay, T.R.; Royer, R.L.; Gao, H.; Zhao, X.; Rose, J.L. A comparison of embedded sensor Lamb wave ultrasonic tomography approaches for material loss detection. *Smart Mater. Struct.* **2006**, *15*, 946–951. [CrossRef]
21. Van Velsor, J.K.; Gao, H.; Rose, J.L. Guided-wave tomographic imaging of defects in pipe using a probabilistic reconstruction algorithm. *Insight Non-Destr. Test. Cond. Monit.* **2007**, *49*, 532–537. [CrossRef]

22. Huthwaite, P.; Simonetti, F. High-resolution guided wave tomography. *Wave Motion* **2013**, *50*, 979–993. [CrossRef]
23. Hettler, J.; Tabatabaeipour, M.; Delrue, S.; Abeele, K.V.D. Linear and nonlinear guided wave imaging of lmpact damage in CFRP using a probabilistic approach. *Materials* **2016**, *9*, 901. [CrossRef] [PubMed]
24. Noo, F.; Defrise, M.; Clackdoyle, R.; Kudo, H. Image reconstruction from fan-beam projections on less than a short scan. *Phys. Med. Biol.* **2002**, *47*, 2525–2546. [CrossRef] [PubMed]
25. Boltz, E.S.; Fortunko, C.M. Absolute sensitivity limits of various ultrasonic transducers. In Proceedings of the Ultrasnics Symposium, Seattle, WA, USA, 7–10 November 1995; Volume 2, pp. 951–954.
26. Robert, E.G. Non-contact ultrasonic techniques. *Ultrasonics* **2004**, *42*, 9–16.
27. Wright, W.M.D.; Hutchins, D.A. Air-coupled ultrasonic testing of materials using broadband pulses in through-transmission. *Ultrasonics* **1999**, *37*, 19–22. [CrossRef]
28. Nishino, H.; Masuda, S.; Yoshida, K.; Takahashi, M.; Hoshino, H.; Ogura, Y.; Kitagawa, H.; Kusumoto, J.; Kanaya, A. Theoretical and Experimental Investigations of Transmission Coefficients of Longitudinal Waves through Metal Plates Immersed in Air for Uses of Air Coupled Ultrasounds. *Mater. Trans.* **2008**, *49*, 2861–2867. [CrossRef]
29. Hutchins, D.A.; Wright, W.; Hayward, G.; Gachagan, A. Air-coupled piezoelectric detection of laser-generated ultrasound. *IEEE Trans. Ultrason. Ferroelectr. Freq. Control.* **1994**, *41*, 796–805. [CrossRef]
30. Gachagan, A.; Hayward, G.; Wright, W.M.D.; Hutchins, D.A. Air coupled piezoelectric detection of laser generated ultrasound. In Proceedings of the Ultrasonics Symposium, Baltimore, MD, USA, 31 October–3 November 1993.
31. Yashiro, S.; Takatsubo, J.; Miyauchi, H.; Toyama, N. A novel technique for visualizing ultrasonic waves in general solid media by pulsed laser scan. *NDT E Int.* **2008**, *41*, 137–144. [CrossRef]
32. Song, B.M.; Kim, J.-H.; Lee, J.-H. Application of laser-generated ultrasound to evaluated wall thinned pipe. In Proceedings of the IVth NDT in Progress, Prague, Czech Republic, 5–7 November 2007; pp. 187–195.
33. Achenbach, J.D. Laser excitation of surface wave motion. *J. Mech. Phys. Solids* **2003**, *51*, 1885–1902. [CrossRef]
34. Arias, I.; Achenbach, J.D. Thermoelastic generation of ultrasound by line-focused laser irradiation. *Int. J. Solids Struct.* **2003**, *40*, 6917–6935. [CrossRef]
35. Choi, S.; Jhang, K.-Y. Influence of slit width on harmonic generation in ultrasonic surface waves excited by masking a laser beam with a line arrayed slit. *NDT E Int.* **2013**, *57*, 1–6. [CrossRef]
36. Cosenza, C.; Kenderian, S.; Djordjevic, B.B.; Green, R.E.; Pasta, A. Generation of narrowband antisymmetric lamb waves using a formed laser source in the ablative regime. *IEEE Trans. Ultrason. Ferroelectr. Freq. Control.* **2006**, *54*, 147–156. [CrossRef] [PubMed]